Neutronic Analysis of Non-Self-Shielded Cyclotron: An Integrated Approach Using Experimental Measurements and Monte Carlo Simulations for In-Depth Assessment

Mohammed A. Alawi[1,2]*, Rayan B. Fawrah[2], Yahya Z. Hazzaa[2], Abdulsalam M. Alhawsawi[2,3,4], Eslam M. Taha[2,3,5], Ezzat Elmoujarkach[6,7], Sarah. Y. Farhood[8], Mona A. Alredhi[8], Mosab A. Balkheir[8], Mohammad A. Sharaf[8], Rakan N. Alsaif[8], Essam M. Banoqitah[2]

* Corresponding author: e-mail: malawi0021@stu.kau.edu.sa; eng.m.alawi@gmail.com - Cell phone: +966557870132

[1] *Mechanical Engineering Department, College of Engineering, King Saud University, Riyadh 4545, Saudi Arabia*

[2] *Nuclear Engineering Department, Faculty of Engineering, King Abdulaziz University, P.O. Box 80204, Jeddah 21589, Saudi Arabia*

[3] *Center for Training & Radiation Protection, King Abdulaziz University, P.O. Box 80204, Jeddah, 21589, Saudi Arabia*

[4] *School of Nuclear Science and Engineering, Oregon State University, Corvallis, OR, 97333, United States*

[5] *School of Engineering, Cardiff University, Cardiff, Wales, UK*

[6] *Institut für Medizintechnik, Universität zu Lübeck, Ratzeburger Allee 160, 23562 Lübeck, Germany*

[7] *Weill Cornell Medicine, Department of Radiology, 525 E 68th St, New York, NY 10065, United States of America*

[8] *I-One Molecular Imaging Center, King Abdulaziz University, P.O.Box 7439-2263, Jeddah 22254, Saudi Arabia*

Abstract

Broad-energy spectrum of neutrons is produced in medical cyclotrons during Fluorine-18 production. In this work, a detailed three-dimensional (3D) spatial neutronic analysis was conducted within a cyclotron facility in the vicinity of a non-self-shielded PETtrace cyclotron target, supported by a GEANT4-based Monte Carlo simulation. Moreover, the presence of a shielding column, made of lead (Pb), which has a relatively high neutron scattering cross-section, was evaluated experimentally. Multiple sets of gold (Au) and cadmium (Cd) foils were used in three arrangements to evaluate the thermal and epithermal neutron fluxes utilizing Neutron Activation Analysis (NAA). The evaluated total neutron fluxes were found to be on the order of 1E+06 neutrons/ cm². sec in the forward direction at all investigated positions. The findings indicate that the area around the target exhibits a high intensity of both thermal and epithermal neutron flux. Operational factors such as routine cyclotron maintenance and increased target volume also contribute to a rise in thermal neutron flux. In addition, the Pb column causes a significant increase in thermal neutron flux, with enhancements reaching up to 86%. The obtained results will serve as a reference for future safety assessments, including estimates of radioactive waste generation and worker dose exposure over the operational lifetime of the cyclotron facility.

Keywords: Neutron Flux, Neutron Activation Analysis, Monte Carlo, Cyclotron, PETtrace.

Itroduction

In recent years, an intense focus has been directed towards accelerator-based instruments as neutron sources for diverse applications. As a result, researchers' efforts have focused on their conceptualization, design optimization and performance characterization [1–14]. In one study [15], the Institute for Plasma Research (IPR) developed a high-yield accelerator-based neutron source, capable of generating neutron fluxes on the order of 10^{12} neutrons/ cm^2. sec, primarily for fusion-related experiments. Monte Carlo simulations were employed to validate experimental measurements and characterize the neutron flux under both pulsed and continuous operation modes. While initial energy-angular distributions were estimated using neutron detectors, future work aims to apply foil activation techniques to enhance the accuracy of angular flux estimations. The application of accelerator-produced neutrons in Boron Neutron Capture Therapy (BNCT) has also been comprehensively examined [16]. This includes discussions on challenges in beam design, collimation, directionality, spatial distribution of thermal neutrons, and patient dose considerations across various accelerator technologies. Another study [17] explored the impact of target material selection and beam operation mode (pulsed vs. continuous) on neutron flux characteristics. Lithium, lithium fluoride, and lithium oxide were evaluated as potential target materials for proton accelerators under thermally controlled conditions. The findings suggest that lithium fluoride and lithium oxide's thermal stability and physical properties contribute favorably to sustained neutron generation in both pulsed and continuous modes.

Medical radioisotope production is achieved through different mechanisms, one of which is cyclotrons. They are charged particle accelerators that work on the principle of accelerating light ions such as protons, deuterons, and helium [18]. Cyclotrons are essential for the production of short-lived and proton-rich radioisotopes for medical applications, academic research, and commercial purposes. The most widely produced isotope in the medical field is Fluorine-18 (^{18}F), by bombarding a target composed of enriched water ($H_2{}^{18}O$) with accelerated protons via the $^{18}O(p, n)^{18}F$ reaction. The collision between the accelerated charged particles and the target in cyclotrons yields different prompt and delayed radiation products, such as photons, neutrons, and charged particles. Neutrons are produced at multiple locations inside the cyclotron, such as the target and the Havar window. The resultant neutrons are categorized into several types: cascade neutrons, evaporation neutrons, and thermal, epithermal, and fast neutrons [19].

When secondary neutrons are produced, most cyclotron facilities face challenges related to the activation of surrounding structural materials, radioactive waste production, and how to benefit from these byproducts.

Efforts have been made to evaluate the neutron characteristics inside cyclotron facilities, utilize the characterized neutron flux in advanced material testing, characterize devices and evaluate neutron flux yields by varying target materials [20–31]. Moreover, considerable attention has been directed toward radioactive waste in the literature. Relatively long-lived radionuclides (e.g., ^{152}Eu, ^{154}Eu, ^{60}Co, and ^{134}Cs) produced by neutron interactions with the surrounding structure and activated air elements (e.g., ^{41}Ar) inside cyclotron facilities were adequately evaluated. Subsequently, insights were provided on the cyclotron facilities design and decommissioning [32–40].

In 2006, according to the Directory of Cyclotrons Used for Radionuclide Production (DCRP) published by the International Atomic Energy Agency (IAEA), approximately 350 cyclotrons are in operation worldwide [41]. By 2020, owing to the increased demand for medical radioisotopes, this number had risen to over 1,300 cyclotrons, according to the IAEA Accelerator Knowledge Portal – Cyclotron Master List [42]. Based on the available data, Saudi Arabia has shown a growing interest in radioisotope production, with 12 cyclotrons either planned, under construction, or currently in operation.

In principle, the lifecycle of a cyclotron comprises several stages, starting with the planning, design, construction, commissioning, operation, and finally decommissioning phases. During the planning, design, and construction phases, special attention must be given to the radiation behavior, particularly the secondary radiation, the neutron flux, and the associated effects due to the activation of surrounding materials. Despite significant research efforts, two key gaps remain in the study of non-self-shielded cyclotrons: 1) the lack of detailed 3D neutronic

characterization near the cyclotron target, and 2) insufficient accounting for scattered neutrons in the presence of high-scattering materials such as Pb.

Despite the relatively high fast neutron flux (>1E+08 neutrons/ cm^2. sec) produced at the target of the PETtrace 880 cyclotron, as reported in several studies [43,44], the present study aims to characterize the thermal and epithermal neutrons in the presence of a high-scattering cross-section material in a medical facility in western Saudi Arabia. Understanding the behavior of neutrons establishes a robust foundation for other cyclotrons in the planning phase and for estimating radioactive waste during the facility decommissioning phase. The Neutron Activation Analysis (NAA), known for its reliability in measuring neutron flux without mechanical, electromagnetic, and temperature influences [45–47], was used in this study.

Methods

3D Printed Array

The nature of the current study necessitates experimental repetition; therefore, ensuring a controlled environment is crucial. Hence, a system that is stable, resilient, and easy to add/remove samples from is preferable to minimize uncertainties and enable reproducibility. One key factor to consider is the interaction of neutrons with the surrounding materials, which induces activation and restricts sample collection and counting. Although there is a straightforward procedure before entering the cyclotron vault, the time is another critical factor. The factors mentioned above were initially considered and implemented in a 3D printed array.

The 3D printed array was constructed entirely from Acrylonitrile Butadiene Styrene (ABS) materials using a 3D printer. ABS is an organic-based material that does not produce long-lived radionuclides when exposed to neutrons. The array has a rectangular shape composed of a base and a holder with several elevations. The base and holder feature evenly spaced openings (2 cm on the base and 1.40 cm on the holder), enabling a wide coverage area, as illustrated in Figure 1. The holder incorporated a flexible operation mechanism for rapid insertion into and removal from the base. Furthermore, the array's unique design addresses safety-related challenges commonly encountered in experimental setups within an environment with a level of activity higher than the background levels (e.g., unnecessary radiation exposure, time of radioactive sample handling inside the cyclotron vault, experiment stability, and repeatability). It also offers a simple indexing system that shows the rows (R), columns (C), and elevation (E), as listed in Table 1.

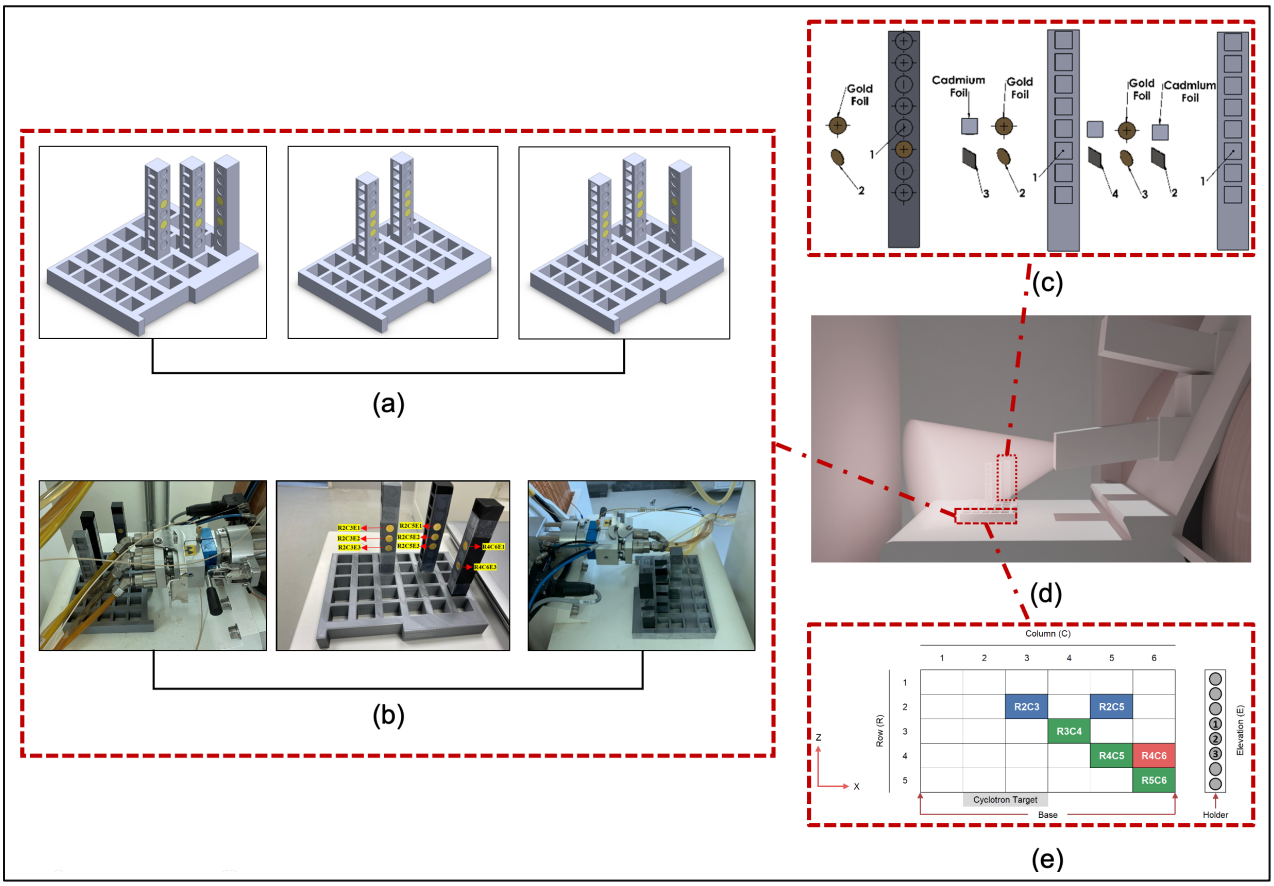

Figure 1: The left-hand side (a) and (b) show a SolidWorks design representation and real application of the three arrangements. The right-hand side (c) displays the bare and cadmium foils placement in the holder and (d) provides a side view demonstration of the direct conically emitted neutrons.

Table 1: Measured activity for bare and Cd-covered gold foils and estimated thermal and epithermal neutron flux for the three arrangements

Arrangement	Sample Position	Activity (Bq)		Neutron Flux (neutrons/ cm^2. sec)	
		Bare Gold	Cd-covered Gold	Thermal	Epithermal
First	R2C3E1	1.72E+03 ± 4.04E+01	9.52E+02 ± 2.38E+01	1.45E+06 ± 8.88E+04	5.84E+05 ± 1.46E+04
	R2C3E2	1.73E+03 ± 4.19E+01	1.24E+03 ± 3.07E+01	9.17E+05 ± 9.84E+04	4.59E+05 ± 1.13E+04
	R2C3E3	1.75E+03 ± 4.25E+01	1.06E+03 ± 2.64E+01	1.34E+06 ± 9.72E+04	6.54E+05 ± 1.63E+04
	R2C5E1	9.41E+02 ± 2.36E+01	1.11E+03 ± 2.74E+01	5.54E+05 ± 1.22E+05	5.73E+05 ± 1.42E+04
	R2C5E2	9.60E+02 ± 2.40E+01	1.07E+03 ± 2.65E+01	3.69E+05 ± 1.23E+05	6.03E+05 ± 1.50E+04
	R2C5E3	1.02E+03 ± 2.54E+01	8.45E+02 ± 2.14E+01	5.84E+05 ± 1.12E+05	6.30E+05 ± 1.59E+04
Second	R2C3E1	1.24E+03 ± 3.06E+01	8.03E+02 ± 2.04E+01	1.15E+06 ± 9.64E+04	5.91E+05 ± 1.50E+04
	R2C3E2	1.18E+03 ± 2.91E+01	7.77E+02 ± 1.98E+01	1.04E+06 ± 9.15E+04	5.67E+05 ± 1.44E+04
	R2C3E3	1.25E+03 ± 3.07E+01	8.78E+02 ± 2.21E+01	1.23E+06 ± 1.27E+05	4.60E+05 ± 1.16E+04
	R2C5E1	1.17E+03 ± 2.90E+01	1.21E+03 ± 3.05E+01	9.40E+05 ± 9.00E+04	6.01E+05 ± 1.50E+04
	R2C5E2	1.15E+03 ± 2.84E+01	8.31E+02 ± 2.10E+01	8.27E+05 ± 9.27E+04	6.12E+05 ± 1.55E+04
	R2C5E3	1.25E+03 ± 3.07E+01	8.36E+02 ± 2.11E+01	1.07E+06 ± 9.74E+04	6.12E+05 ± 1.55E+04
	R4C6E1	1.11E+03 ± 2.74E+01	7.65E+02 ± 1.95E+01	9.03E+05 ± 8.92E+04	5.69E+05 ± 1.45E+04
	R4C6E3	1.22E+03 ± 3.00E+01	7.94E+02 ± 2.01E+01	1.12E+06 ± 9.57E+04	5.90E+05 ± 1.50E+04
Third	R3C4E1	1.34E+03 ± 3.20E+01	9.79E+02 ± 2.84E+01	9.60E+05 ± 1.10E+05	7.19E+05 ± 1.80E+04
	R3C4E3	1.42E+03 ± 3.40E+01	9.99E+02 ± 3.27E+01	1.11E+06 ± 1.10E+05	7.31E+05 ± 1.80E+04
	R4C5E1	1.23E+03 ± 3.00E+01	9.55E+02 ± 2.84E+01	8.00E+05 ± 1.10E+05	7.39E+05 ± 1.80E+04

	R4C5E3	1.43E+03 ± 3.40E+01	1.03E+03 ± 3.25E+01	1.09E+06 ± 1.20E+05	7.64E+05 ± 1.90E+04
	R5C6E1	1.14E+03 ± 2.80E+01	8.23E+02 ± 2.84E+01	9.10E+05 ± 1.00E+05	6.27E+05 ± 1.60E+04
	R5C6E3	1.32E+03 ± 3.20E+01	8.46E+02 ± 2.76E+01	1.27E+06 ± 1.00E+05	6.28E+05 ± 1.60E+04

Two approaches were followed to optimize the experimental setup and ensure accurate results. The first approach was implemented during a preliminary investigation phase, and it involved placing holders separately to identify spots suitable for further investigation. The second approach involved simultaneously inserting three holders simultaneously in the selected spots to ensure that the samples experienced similar irradiation conditions.

Foils selection

The foil activation technique was employed in this study to understand the behavior of the neutron field. It can reveal key details related to three energy regions in a neutron spectrum: thermal, epithermal, and fast [48–52]. Pure gold foils from ESPIMetals® (gold foil 0.004" 3n5) with masses ranging from 0.1531 to 0.1570 grams were chosen because of their high thermal and epithermal neutron capture cross-sections [53,54]. The gold foils were cylindrical, with diameters and thicknesses of 1 cm and 100 µm, respectively. Cadmium foils were introduced into the experiments to filter thermal neutrons and evaluate the epithermal neutrons. The cadmium filters were cubes with a 1 cm^2 area and 1 mm thickness.

Shielding Column

At a distance of 60 cm from the target, a fixed Pb column is shown in Figure 2. The Pb column thickness, width, and height were 15, 70, and > 200 cm, respectively. Behind the column, cyclotron workers perform routine activities that require their presence for short intervals, such as refilling the target with ($H_2{}^{18}O$) after multiple runs. The Pb column played a vital role in preventing neutrons from traversing through and interacting with the concrete wall behind it. This preventive measure effectively reduced the buildup of activities after each run. Nevertheless, despite the effectiveness of the Pb column in reducing the activity, it still has a high neutron elastic scattering cross-section, as shown in Figure 3.

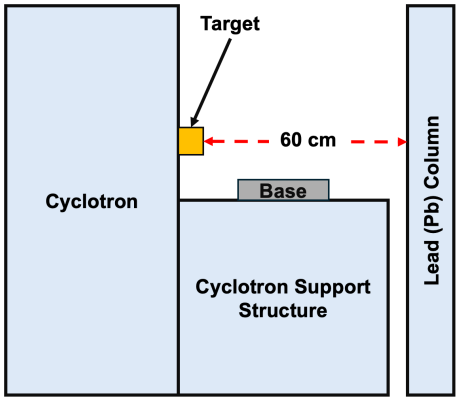

Figure 2: Cross-sectional view of cyclotron structure

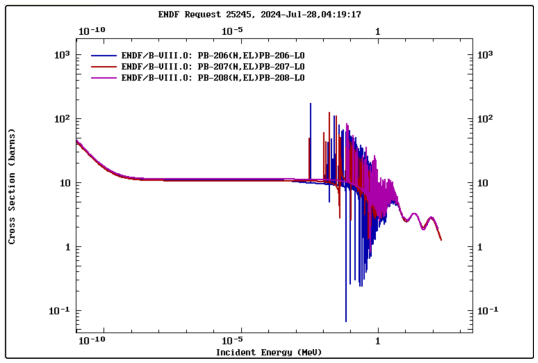

Figure 3: Lead (Pb) neutron elastic scattering cross-section data obtained from the IAEA Evaluated Nuclear Data File (ENDF) library

Experiments Procedure

The cyclotron understudy is a non-self-shielded type with an energy of 16.5 MeV. It operates three to four days per week with an average current of 65 µAmp per run. Eight (8) bare gold foils and (16) cadmium foils were used during the experiments. The position of the holder

facing the target was selected to be 10 cm away, and the minimum allowable distance was set according to the cyclotron operator's recommendation. Upon scrutinizing the different setups, as shown in Figure 1 (c), the ones applied in this work are: 1) placing the bare gold foils in the selected position and irradiating them, 2) placing the Cd foils in front of the bare gold foils in the direction facing the cyclotron's target, and 3) placing the Cd foils in front and behind the bare Au foils in a sandwich setup.

Three arrangements were proposed for evaluating the neutron field, as shown in Figure 1. In the first arrangement, two holders were inserted at the R2C3 and R2C5 positions, each with the gold foils placed at three elevations. The second arrangement was performed with the addition of another holder to R4C6, thereby expanding the range of investigation. In the second arrangement, three gold foils were placed at R2C3 and R2C5, and two foils were placed at R4C6. Moreover, the second arrangement was performed under different circumstances, in which routine maintenance tasks were performed before the irradiation. The third arrangement followed a diagonal formation, occupying R3C4, R4C5, and R5C6, with two gold foils placed at the first and third elevations. The first two arrangements focused on investigating the direct neutron flux simultaneously to generate a spatial map. The third (diagonal) arrangement, located near one of the cyclotron walls, investigated the direct and the scattered neutron fluxes separately, providing critical inputs for subsequent studies on concrete activation and decommissioning.

The dose rate monitoring system mounted on the wall inside the cyclotron vault indicated that the induced activity immediately after the run was greater than 200 μSv/hr. Therefore, the foils were left in the 3D printed holder inside the vault for 12 to 24 hours after each irradiation to avoid unnecessary radiation exposure. The activated gold (^{198}Au) foils were then collected, and the gamma rays emitted at 411 keV were measured using a calibrated Broad Energy Germanium (BEGe) detector. The measured responses for the three arrangements were adjusted using decay correction factors corresponding to the duration from the end of irradiation until the counting time began, as well as other corrections during sample preparation.

Monte Carlo Simulation

The Geant4 Application for Emission Tomography (GATE) toolkit, version 9.1, was used to validate the experimental results. Gate is a Monte Carlo-based, open-source software dedicated to numerical simulations [55]. The simulation setup was conservative and focused on a cubical geometry measuring 30 × 30 × 30 cm, covering the area between the target and the Pb column. To reduce computation time, the setup did not include the Pb column or other surrounding structures. Instead, it was designed to calculate the thermal and epithermal neutron flux values in Cartesian coordinates, with a spatial resolution of 1 cm in the x, y, and z directions.

Statistical and Systematic Sources of Uncertainty

Multiple sources of uncertainty influence the accurate characterization of neutron fluxes. In neutron flux measurements based on neutron activation, uncertainties arise from both experimental (statistical) and systematic (physical and modeling) sources. Experimental uncertainties include statistical counting errors, gamma-ray detector efficiency calibration, uncertainties in foil mass and positioning, irradiation and cooling times, and counting geometry, and uncertainties associated with nuclear decay data and detector response [56]. Standard error-propagation techniques were applied to quantify the combined contribution of these statistical uncertainties.

In addition, systematic uncertainties are introduced during the conversion of measured activities into neutron flux values. These uncertainties are mainly associated with assumptions regarding energy-dependent neutron capture cross sections, spectral weighting in the thermal and epithermal energy regions, and the effective cadmium cutoff energy. Also, Monte Carlo-based simulations introduce additional model-related uncertainties associated with physics models, material compositions, and assumptions on the neutron energy spectrum. The combined impact of these statistical and systematic uncertainties directly impacts the reported neutron flux values and is accounted for in the final uncertainty estimates.

Results and Discussion

Experimental Measured Response

The responses of the first arrangement demonstrated a 50% increase in the count rate in the first position (R2C3) compared to the second position (R2C5) for bare foils. The Cd-covered foil count rate increased by 20% in the first position compared to that in second position. Furthermore, analogous observations were made at each position across the three elevations. The observed increase in the count rate at the first position suggested that the bare foils were exposed to a high thermal neutron flux. In contrast, the unchanged pattern in the count rate in Cd-covered foils suggests a constant exposure to epithermal flux for both positions.

The responses of the second arrangement revealed a consistent pattern in which the count rate remained nearly identical among the three positions and across each elevation for both the bare and Cd-covered foils. Overall, the second arrangement has demonstrated a balanced exposure to thermal and epithermal neutron fluxes. The responses of the third arrangement demonstrated variations among all positions, with a notable increase in the first position for the Cd-covered foil, and an increase in the count rate at the third position for the bare foils. This observation indicates that the thermal neutron flux component significantly contributes to this arrangement, particularly at the third elevation, more so than the epithermal flux. The calculated activities for the three arrangements are presented in Table 1 and are shown in Figure 4.

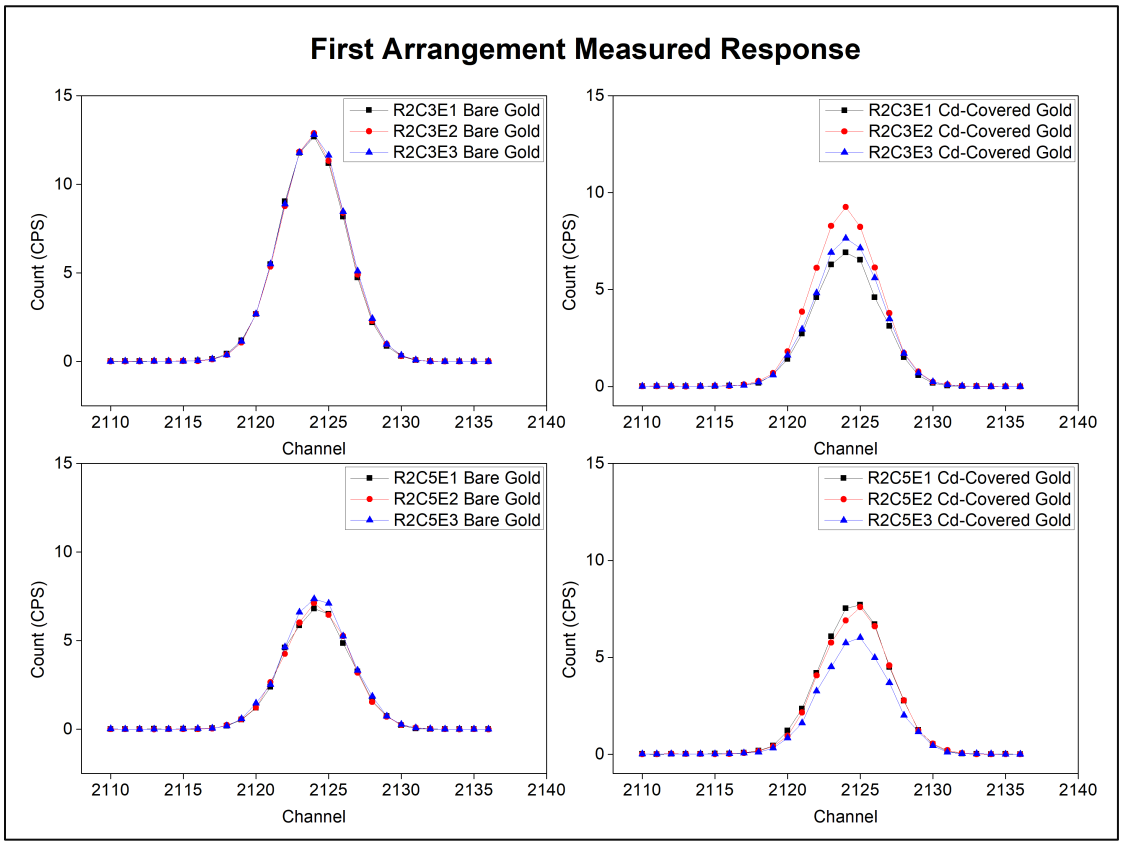
First Arrangement Measured Response
R2C3E1 Bare Gold
R2C3E2 Bare Gold
R2C3E3 Bare Gold
R2C3E1 Cd-Covered Gold
R2C3E2 Cd-Covered Gold
R2C3E3 Cd-Covered Gold
R2C5E1 Bare Gold
R2C5E2 Bare Gold
R2C5E3 Bare Gold
R2C5E1 Cd-Covered Gold
R2C5E2 Cd-Covered Gold
R2C5E3 Cd-Covered Gold
Count (CPS)
Channel
0
5
10
15
2110
2115
2120
2125
2130
2135
2140

(a)

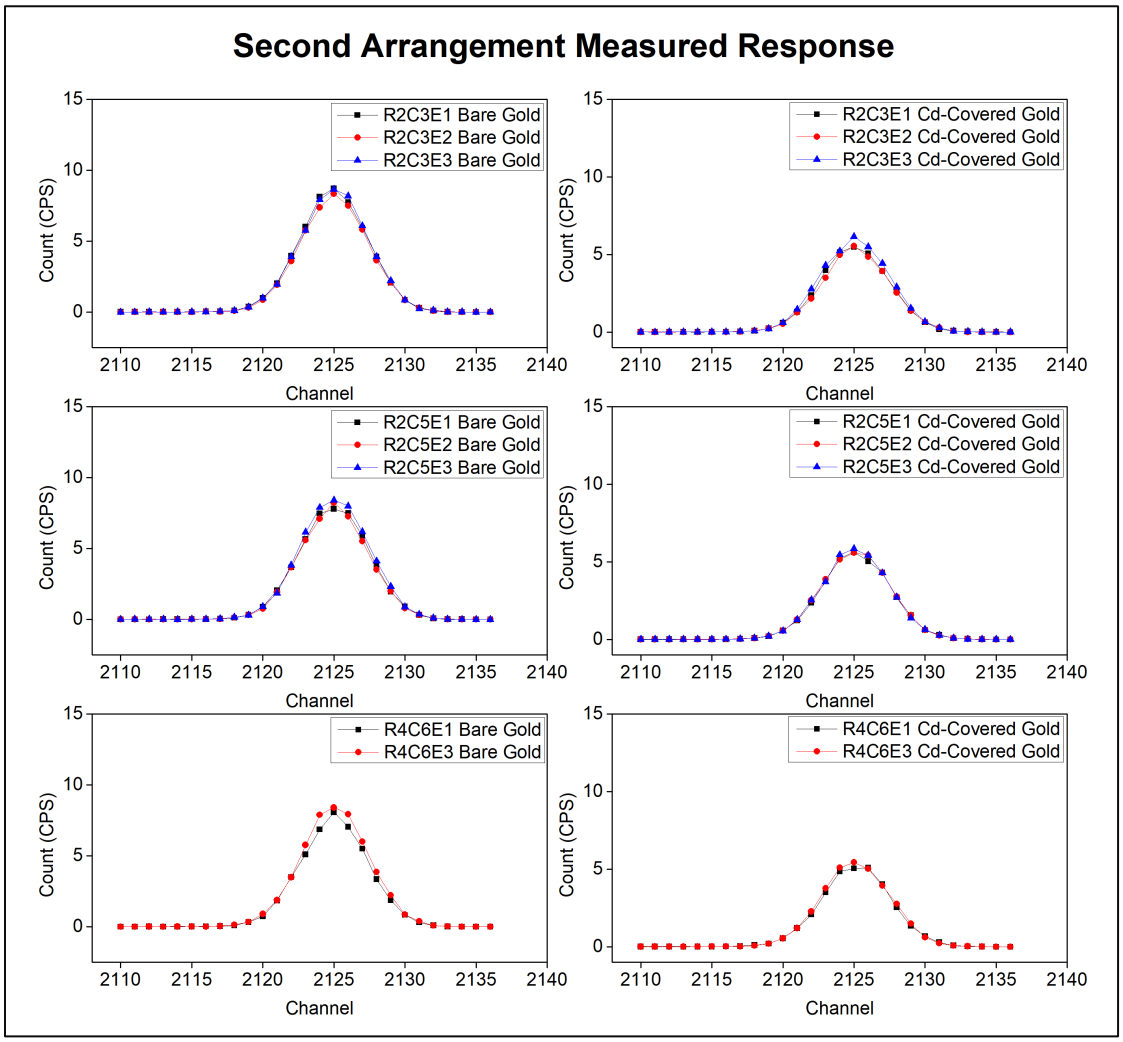
Second Arrangement Measured Response
R2C3E1 Bare Gold
R2C3E2 Bare Gold
R2C3E3 Bare Gold
R2C3E1 Cd-Covered Gold
R2C3E2 Cd-Covered Gold
R2C3E3 Cd-Covered Gold
R2C5E1 Bare Gold
R2C5E2 Bare Gold
R2C5E3 Bare Gold
R2C5E1 Cd-Covered Gold
R2C5E2 Cd-Covered Gold
R2C5E3 Cd-Covered Gold
R4C6E1 Bare Gold
R4C6E3 Bare Gold
R4C6E1 Cd-Covered Gold
R4C6E3 Cd-Covered Gold
Count (CPS)
Channel
0
5
10
15
2110
2115
2120
2125
2130
2135
2140

(b)

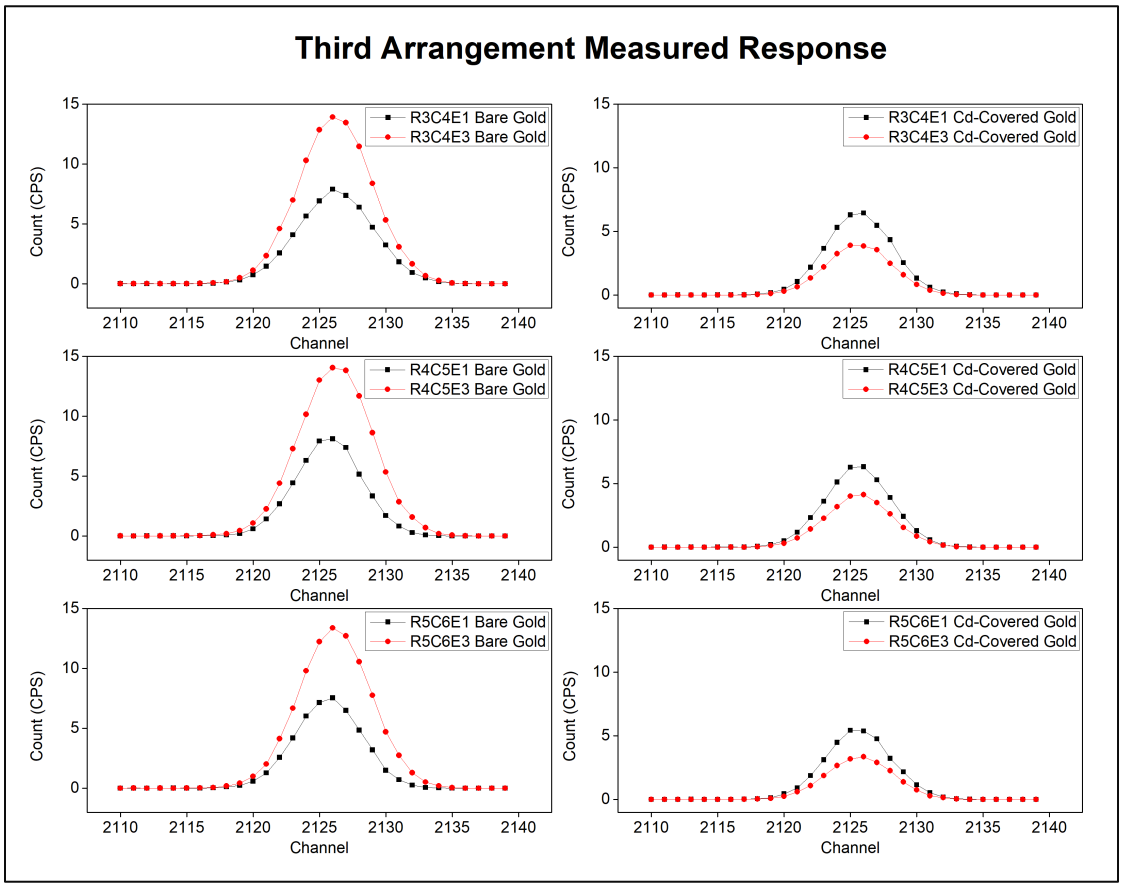

(c)

Figure 4: The measured responses from the activated Au foil at 411 keV peaks with and without Cd filters for the first (a), second (b) and third (c) arrangements

Experimental Neutron Flux Evaluation

After performing more than 60 irradiation experiments, the measured responses of the activated gold foils were converted into activity. Subsequently, the thermal and epithermal neutron fluxes were estimated using the methodology and equations established in a previous study conducted at the same cyclotron facility [57]. The estimated thermal and epithermal neutron flux values are presented in Table 1, and shown in Figure 5 and Figure 6.

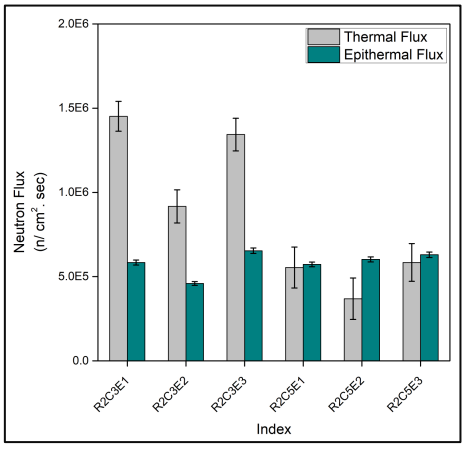

(a)

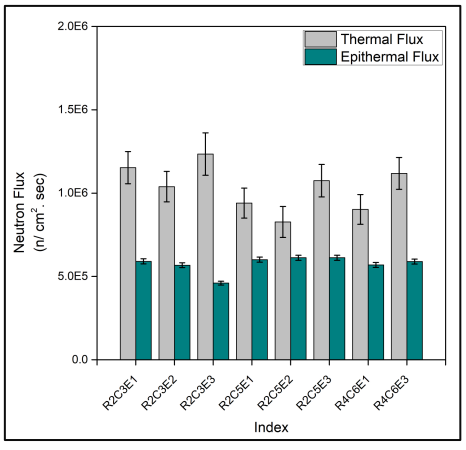

(b)

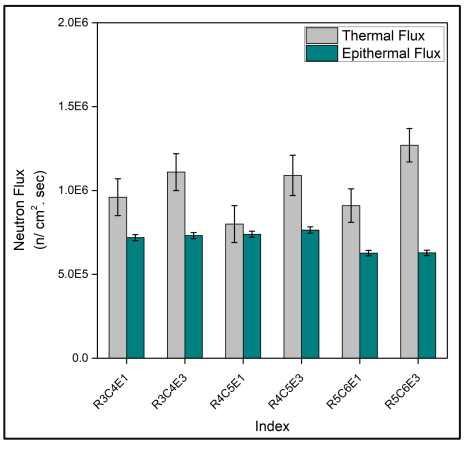

(c)

Figure 5: Estimation of thermal and epithermal neutron flux of the first (a), second (b) and third (c) arrangements

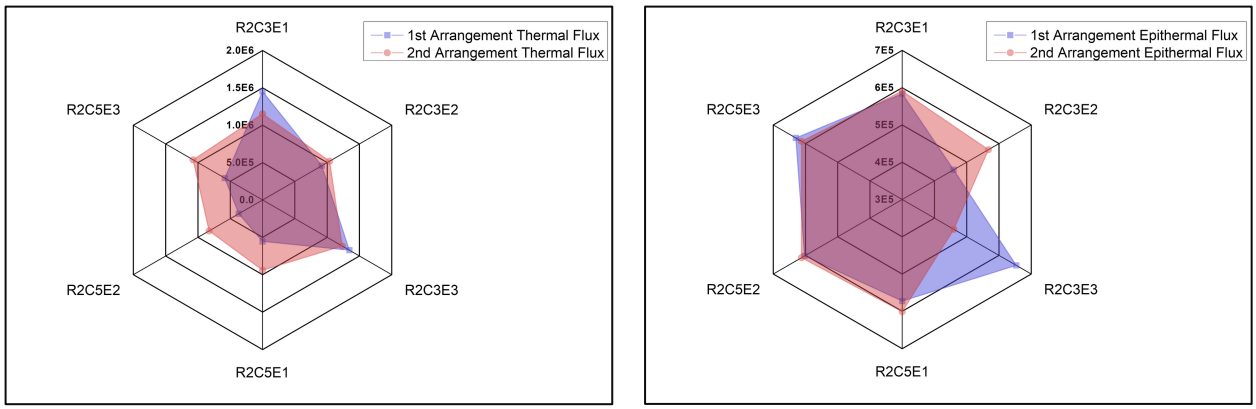

(a) (b)

Figure 6: Comparison of the first and second arrangements estimated neutron flux (in neutrons/ cm^2. sec) at R2C3 and R2C5

First Arrangement

The experiment was designed to account for most neutrons emitted in the forward direction. According to the manufacturer's manual [58], approximately 90% of the neutrons are emitted in the forward direction from the cyclotron target. Therefore, based on the recommendations of the cyclotron operator, the selected positions, R2C3 and R2C5, were deemed suitable. The distance between the target and the holder at R2C3 was 10 cm from the target, which was regarded as the minimum allowed distance to place any object. Across all three elevations at R2C3, high thermal neutron flux and comparable epithermal flux values were observed compared with the R2C5 position, as shown in Figure 6 (a). The highest estimated values of the thermal and epithermal neutron fluxes were 1.45E+06 ± 8.88E+04 neutrons/ cm^2. sec in the first elevation at the first position and 6.54E+05 ± 1.63E+04 neutrons/ cm^2. sec at the third elevation at the first position.

Second Arrangement

This arrangement was analogous to the first arrangement, with the addition of one holder at the R4C6 position. The experiment was repeated to study the influence on the neutron flux caused by two factors: 1) performance of some routine maintenance tasks after the first arrangement experiment, which included replacement of the Havar foil, replacement of O-rings, and increases in the volume of the target by 0.3% to enhance the yield of the production, and 2) some operational factors such as the period between the two experiments of three months, and the cyclotron reported mean current changed slightly between each experiment. These factors collectively contributed to a measurable increase of 47% in the average thermal neutron flux at the R2C5 position compared to the same position in the first arrangement, as shown in Figure 6 (b) and Figure 7. In contrast, the average epithermal neutron flux showed an insignificant change, and it was assumed that routine maintenance tasks influenced the improvement in the thermal neutron flux in this arrangement. Furthermore, unlike the first arrangement, the thermal neutron flux indicated higher values at the R2C3 and R3C5 positions. The highest estimated values of the thermal and epithermal neutron fluxes were 1.23E+06 ± 1.27E+05 neutrons/ cm^2. sec in the third elevation at the first position and 6.12E+05 ± 1.55E+04 neutrons/ cm^2. sec at the second and third elevations, respectively, at the second position. However, the factors mentioned earlier must be investigated separately to confirm the significance of their impact. Further analysis showed that the newly added position (R4C6) thermal and epithermal neutron flux values agree with the values of the other two positions.

Third Arrangement

In this arrangement, three positions (R3C4, R4C5, and R5C6) were proposed and only two elevations were examined at each of these positions. The arrangement showed a significant thermal neutron flux contribution, particularly at the third elevation, in all positions.

However, the thermal neutron flux did not exhibit a significant increase compared with the other arrangements. The epithermal neutron flux exhibited a stable behavior within this arrangement, and among other arrangements. As shown in Figure 5 (c), the peak thermal and epithermal fluxes were 1.27E+06 ± 1.00E+05 neutrons/ cm^2. sec at the third elevation at the third position and 7.64E+05 ± 1.90E+04 neutrons/ cm^2. sec in the third elevation at the second position, respectively.

The scattered neutron flux values at the same positions with selected elevations, provided in Table 2, were evaluated in a previous study to explore their contribution to the total neutron flux value [59]. However, the study deduced that the backscattered neutrons were found to increase the total neutron flux by 43–86%.

Table 2: Estimated scattered thermal and epithermal neutron flux in the third arrangement

Arrangement	**Sample Position**	**Neutron Flux (neutrons/ cm^2. sec)**	
		Thermal	**Epithermal**
Third	R3C4E1	4.10E+05 ± 1.20E+05	7.48E+05 ± 1.80E+04
	R3C4E3	1.30E+05 ± 1.30E+05	8.58E+05 ± 2.10E+04
	R4C5E3	1.80E+05 ± 1.30E+05	8.66E+05 ± 2.10E+04
	R5C6E3	4.50E+05 ± 1.10E+05	7.30E+05 ± 1.80E+04

Neutron Flux Spatial Map

The spatial behavior of the thermal and epithermal neutron fluxes was obtained as a function of the distance from the target, as demonstrated in Figure 7. The target was assumed to be located at the center of a rectangular area, divided into four equal quadrants. The first and second quadrants cover most of the emitted neutrons in the forward direction, whereas the third and fourth quadrants represent the neutrons in the backward direction. Due to the structural limitations in the vicinity of the target, the investigated area was selected as the second quadrant. Because of the isotropic nature of the emitted neutrons, quadrants one and two are assumed to have the same exposure from the neutrons; hence, quadrant one has the same measured values as quadrant two. According to the General Electric PETtrace cyclotron site planning guide [58], neutrons in the backward direction are ten times lower than the neutrons produced in the forward direction. Consequently, the calculated values in the third and fourth quadrants were conservatively reduced by a factor of ten, neglecting the angular emission impact.

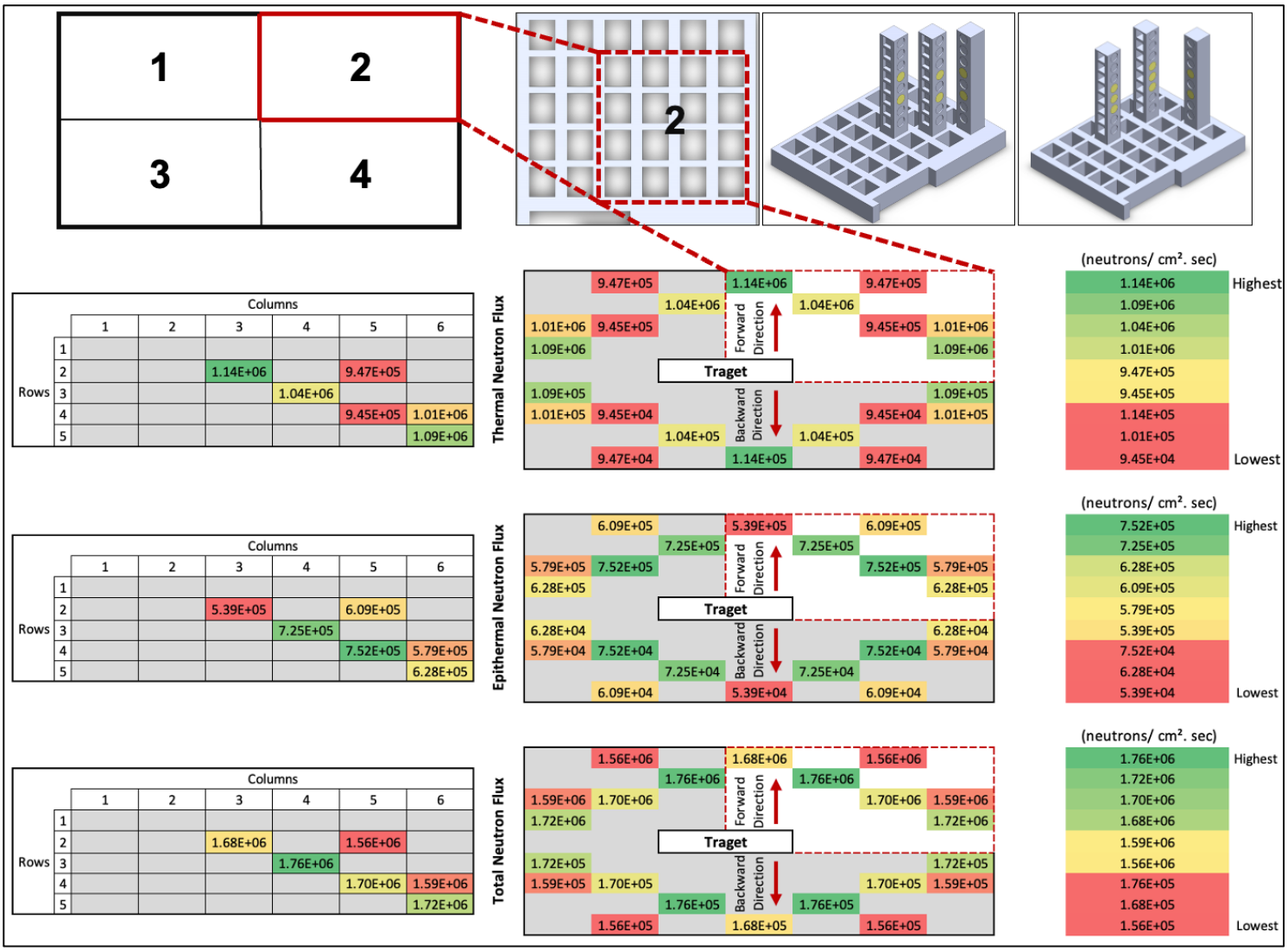

Figure 7: 2D Spatial map for the measured thermal, epithermal and total neutron flux around the target

The R2C3 position registered the highest thermal neutron flux value, whereas the R4C5 position had the lowest. The maximum and minimum epithermal flux values were observed in the diagonal formations at the R4C5 and R2C3 positions, respectively. The findings showed that the total neutron flux values were of the same order of magnitude at all positions. The thermal, epithermal, and total neutron flux values were averaged for each position, as listed in Table 3. Moreover, as shown in Figure 8, the simulation output indicated results on the order of 1E+07 neutrons/ cm^2. sec.

It should be noted that these Monte Carlo simulations were primarily intended to validate spatial distribution trends and relative flux behavior, rather than to provide absolute flux quantification. The observed discrepancy between the simulated values (10^7) and the experimental result (10^6) can be mainly attributed to the idealization of the simulation model. Specifically, the model geometry relied on manual measurements of the experimental setup, which simplified the complex arrangement of surrounding structural materials and introduced positional inaccuracies. Additionally, the simulation assumes a theoretical neutron yield and an idealized source definition, which does not account for experimental losses such as target degradation, beam current instabilities, or detector efficiency limitations.

Table 3: Mean thermal, epithermal, and total neutron flux values at all investigated positions. The values at the R2C3, R2C5, and R4C6 positions refer to the first and second arrangement, and the values at the R3C4, R4C5, and R5C6 positions refer to the third arrangement

Position	Mean Thermal Flux (neutrons/ cm^2. sec)	Mean Epithermal Flux (neutrons/ cm^2. sec)	Total Flux (neutrons/ cm^2. sec)
R2C3	1.14E+06 ± 1.84E+05	5.39E+05 ± 2.38E+04	1.68E+06 ± 1.85E+05
R2C5	9.47E+05 ± 1.62E+05	6.09E+05 ± 2.65E+04	1.56E+06 ± 1.64E+05
R3C4	1.04E+06 ± 1.56E+05	7.25E+05 ± 2.55E+04	1.76E+06 ± 1.58E+05
R4C5	9.45E+05 ± 1.63E+05	7.52E+05 ± 2.62E+04	1.70E+06 ± 1.65E+05
R4C6	1.01E+06 ± 1.31E+05	5.79E+05 ± 2.08E+04	1.59E+06 ± 1.32E+05
R5C6	1.09E+06 ± 1.41E+05	6.28E+05 ± 2.62E+04	1.72E+06 ± 1.43E+05

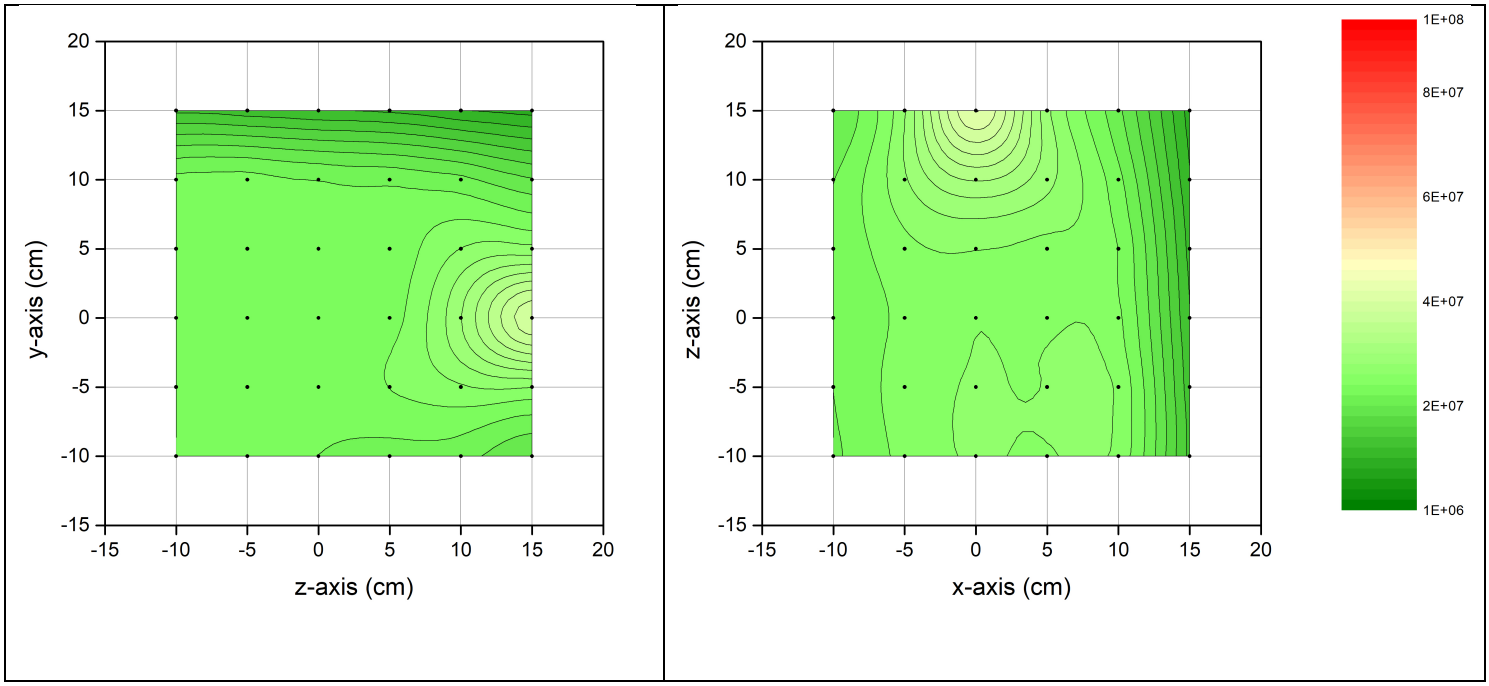

Figure 8: Constructed 2D neutron flux map from the simulation output, where the bar on the right-hand side shows the neutron flux (in neutrons/ cm^2. sec).

Shielding Column

The above evaluation established a baseline for the neutron flux values near the PETtrace 880 cyclotron target. However, the effect of positioning the Pb column in front of the target has not yet been fully correlated with the measured flux. Notably, the Pb, which has a high elastic scattering cross-section, is located close to the target, and the emitted neutrons span a broad energy spectrum, including thermal, epithermal, and fast neutrons.

The 3D printed array used in the experiments consists primarily of low-Z organic materials, such as carbon and hydrogen, which can influence neutron moderation. As illustrated in Figure 9, three sample configurations were implemented in the third arrangement to investigate both direct and scattered neutrons. All configurations shared the base structure of the bare Au foil and holder layers:

- Configuration 1 (baseline): included only the Au foil and holder layers, allowing unfiltered interactions with all incident neutrons.
- Configuration 2: included a Cd layer facing the target that selectively absorbed thermal neutrons from the target direction.
- Configuration 3: built upon the previous layers and an additional Cd layer facing the Pb column, stopping thermal neutrons from both the target and Pb directions.

The ABS layer functioned as a neutron moderator, slowing down higher-energy neutrons and thereby increasing the probability of thermal neutron interaction with the Au foil.

It is also necessary to mention that the observed enhancement (43–86%) of the neutron flux in the third arrangement is bounded by the selected spatial orientation and current geometry of the Pb column relative to the target and the 3D printed array.

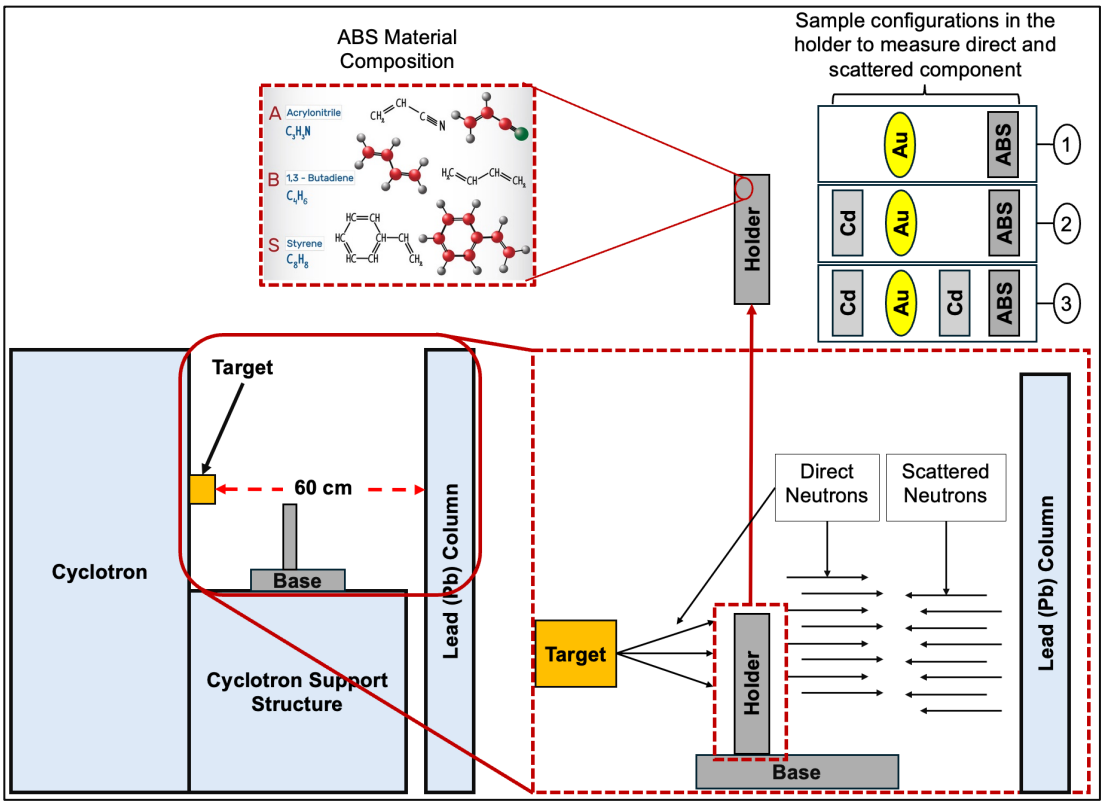

Figure 9: Schematic representation of the sample configurations and corresponding neutron component contributions near the cyclotron target.

Conclusion

Thermal and epithermal neutron flux values were evaluated at multiple locations in a 3D printed array close to the non-self-shielded PETtrace cyclotron target. The highest total average neutron flux value was 1.76E+06 neutrons/ cm^2. sec at the R3C4 position. The distribution of the mean neutron fluxes was found to be of the same order of magnitude at all positions. This finding suggests that the area around the target is rich in thermal and epithermal neutron fluxes, and the measured values are comparable to those of the research reactors. Moreover, it is assumed that routine maintenance tasks and an increase in the target volume influenced the improvement in the thermal neutron flux. In addition, owing to the relatively high elastic cross-section of Pb in the third arrangement, the Pb column significantly increased the thermal neutrons at the selected spots by 43-86%. While the trend of neutron flux enhancement by Pb scattering is consistent, the magnitudes of these values depend on the current installation and may vary across different cyclotron setups. In addition to the neutron flux enhancement, the target's primary fast neutron field holds significant potential for fast neutron irradiation. These features position the PETtrace target as a versatile tool for both fast and thermal neutron research.

With this neutron flux, several projects can be initiated, such as an in-depth concrete and cyclotron structure activation assessment to estimate the waste production and doses inside the cyclotron vault, constructing an NAA facility using the cyclotron target, and performing radiography and material testing. However, the NAA facility requires a unique configuration with a focused neutron beam and uniform neutron flux. However, through the unfolding techniques, the generated fast neutron flux needs to be characterized using materials other than gold with high cross-sections for fast neutron ranges.

Acknowledgements

The authors declare that they have no conflicts of interest related to the content of this manuscript. No financial support or funding was received for the completion of the study.

The authors extend their sincere appreciation to the staff of the Molecular Imaging Center (I-ONE) for their invaluable support and assistance throughout the course of this research. Their technical expertise, availability, and collaborative efforts were instrumental in the successful execution of the experimental work and overall progress of the study.

References

[1] D. D. Dijulio, C. P. Cooper-Jensen, H. Björgvinsdóttir, Z. Kokai, and P. M. Bentley, High-energy in-beam neutron measurements of metal-based shielding for accelerator-driven spallation neutron sources, Physical Review Accelerators and Beams 19, (2016).

[2] A. J. Kreiner et al., Present status of Accelerator-Based BNCT, Reports of Practical Oncology and Radiotherapy 21, 95 (2016).

[3] J. M. Carpenter, *The Development of Compact Neutron Sources*, Nature Reviews Physics.

[4] T. Brückel, T. Gutberlet, S. Schmidt, C. Alba-Simionesco, F. Ott, and A. Menelle, Low energy accelerator-driven neutron facilities—A prospect for a brighter future for research with neutrons, Neutron News 31, 13 (2020).

[5] Y. Wang, D. Chen, R. dos S. Augusto, J. Liang, Z. Qin, J. Liu, and Z. Liu, *Production Review of Accelerator-Based Medical Isotopes*, Molecules.

[6] M. K. Hossain, Md. A. Taher, and M. K. Das, Understanding Accelerator Driven System (ADS) Based Green Nuclear Energy: A Review, World Journal of Nuclear Science and Technology 05, 287 (2015).

[7] S. H. Kim et al., Overview of ten-year operation of the superconducting linear accelerator at the Spallation Neutron Source, Nucl Instrum Methods Phys Res A 852, 20 (2017).

[8] Y. Ikeda, A. Taketani, M. Takamura, H. Sunaga, M. Kumagai, Y. Oba, Y. Otake, and H. Suzuki, Prospect for application of compact accelerator-based neutron source to neutron engineering diffraction, Nucl Instrum Methods Phys Res A 833, 61 (2016).

[9] I. Hofmann, *Review of Accelerator Driven Heavy Ion Nuclear Fusion*, Matter and Radiation at Extremes.

[10] T. Kobayashi, S. Ikeda, Y. Otake, Y. Ikeda, and N. Hayashizaki, Completion of a new accelerator-driven compact neutron source prototype RANS-II for on-site use, Nucl Instrum Methods Phys Res A 994, (2021).

[11] Y. Kiyanagi, *Neutron Imaging at Compact Accelerator-Driven Neutron Sources in Japan*, Journal of Imaging.

[12] M. Uesaka and H. Kobayashi, *Compact Neutron Sources for Energy and Security*, in *Reviews of Accelerator Science and Technology: Volume 8: Accelerator Applications in Energy and Security* (World Scientific Publishing Co., 2017), pp. 181–208.

[13] Y. Kiyanagi, Accelerator-based neutron source for boron neutron capture therapy, Ther Radiol Oncol 2, 55 (2018).

[14] Y. Kiyanagi, *Neutron Applications Developing at Compact Accelerator-Driven Neutron Sources*, AAPPS Bulletin.

[15] M. Abhangi, S. Vala, H. L. Swami, R. Kumar, A. Saxena, and R. Kumar, Neutron emission characterization of IPR 14 MeV neutron generator, Fusion Engineering and Design 204, 114522 (2024).

[16] S. Green, B. Phoenix, S. Nakamura, Y. H. Liu, D. Shu, N. Hu, S. Suzuki, H. Koivunoro, H. Kumada, and H. Tanaka, Accelerator neutron sources for BNCT: Current status and some pointers for future development, Applied Radiation and Isotopes 217, (2025).

[17] S. H. Li, S. Pavlov, Y. Cherepennikov, P. Glumac, M. Zhuravlev, G. Kurapov, A. Bukharkin, and G. Remnev, Estimation of the neutron yield generated by neutron source based on pulsed power proton accelerator in 7Li(p, n)7Be reaction, Nucl Instrum Methods Phys Res A 1075, (2025).

[18] P. Schmor, Review of cyclotrons for the production of radioactive isotopes for medical and industrial applications, Reviews of Accelerator Science and Technology: Accelerator Applications in Industry and the Environment 4, 103 (2012).

[19] H. R. Vega-Carrillo, Neutron energy spectra inside a PET cyclotron vault room, Nucl Instrum Methods Phys Res A 463, 375 (2001).

[20] N. Hu et al., Clinical evaluation of performance, stability, and longevity of an accelerator system designed for boron neutron capture therapy utilising a beryllium target, Nucl Instrum Methods Phys Res A 1072, (2025).

[21] H. W. Park, S. Kang, Y. S. Yoon, H. Park, J. Kim, J. H. Kim, J. Jegal, D. W. Jeong, and H. Kim, Silicon detector characterisation for monoenergetic neutron measurements using proton-recoil telescopes, Nucl Instrum Methods Phys Res A 1065, (2024).

[22] E. Gover, D. Veske, and M. B. Demirkoz, Geant4 and FLUKA Simulations of a Cyclotron Based 30 MeV Proton-Beryllium Reaction: Benchmarking and Optimization of Neutron Fields, (2025).

[23] J. F. Muraz et al., Development of a high current electron beam facility for compact accelerator neutron source target thermal tests, Nucl Instrum Methods Phys Res A 1062, (2024).

[24] M. Zmeškal, M. Košťál, T. Czakoj, J. Šimon, M. Majerle, V. Zach, O. Lebeda, Š. Vadják, M. Antoš, and Z. Matěj, Characterization of the secondary neutron field inside a cyclotron for production of radiopharmaceuticals, Applied Radiation and Isotopes 199, (2023).

[25] L.-F. Chen, S.-L. Jeng, C.-S. Tsao, and J.-S. Tsay, Machine Learning-Based Design and Monte Carlo Simulation of a Neutron Beam Shutter for Cyclotron-Based Neutron Sources, (2025).

[26] S.-L. Jeng, H.-M. Lee, Y.-H. Teng, Y.-H. Hsu, C.-H. Chen, W.-S. Kuo, and T.-S. Duh, The cyclotron-based neutron sources and projects at NARI, EPJ Web Conf 298, 04001 (2024).

[27] D. W. Lee, K. Lee, B. Jung, J. Lee, J. H. Park, J. Kim, M. K. Moon, and C. H. Lee, Development status of 30 MeV cyclotron-based neutron source in Korea, EPJ Web Conf 298, 05004 (2024).

[28] V. O'Donnell, T. Keya, A. Romans, M. Andurkar, B. C. Prorok, S. M. Thompson, and J. Gahl, Novel method for fast neutron irradiation of materials via positron emission tomography isotope producing cyclotron, Radiation Physics and Chemistry 212, (2023).

[29] R. Tursinah et al., Characterization of proton-induced neutron spectrum on Ti-nat target in 11 MeV cyclotron using a passive single moderator neutron spectrometer, Radiation Physics and Chemistry 227, (2025).

[30] B. D. Jeffries, C. Algiere, J. A. Gallagher, T. H. Nichols, J. R. So, C. W. Littlefield, M. Quinn, and J. D. Brockman, Characterization of the neutron flux during production of 18F at a medical cyclotron and evaluation of the incidental neutron spectrum for neutron damage studies, Applied Radiation and Isotopes 154, (2019).

[31] H. Shim and S. H. Park, Study of accelerator-based epithermal neutron flux depending on Li and Be targets, Applied Radiation and Isotopes 208, (2024).

[32] V. Bonvin, F. Bochud, J. Damet, C. Theis, H. Vincke, and R. Geyer, Detailed study of the distribution of activation inside the magnet coils of a compact PET cyclotron, Applied Radiation and Isotopes 168, (2021).

[33] J. Collin, J. Horodynski, N. Arbor, M. Barbagallo, F. Carminati, G. G. Carminati, and L. J. Tagliapietra, Validation of Monte Carlo simulations by experimental measurements of neutron-induced activation in cyclotrons, EPJ Web Conf 04025, (2023).

[34] H.-S. L. Mahdi Bakhtiari, Leila Mokhtari Oranj , Nam-Suk Jung, Arim Lee, Study on Concrete Activation Reduction in a PET Cyclotron Vault, Journal of Radiation Protection and Research 45, 130 (2020).

[35] A. A. Abuhoza, H. A. Kassim, A. A. Alghamdi, F. M. Alrumayan, M. Arib, I. J. Aljammaz, and M. Alqahtani, Identification of Activation Isotopes in a CS-30 Cyclotron Vault, Sensors (2022).

[36] V. Bonvin, F. Bochud, C. Theis, H. Vincke, J. Damet, and R. Geyer, A combined approach for the calculation of activation yields and the characterization of materials for a medical cyclotron, Applied Radiation and Isotopes 204, (2024).

[37] E. Ionescu, D. Gurau, D. Stanga, M. Dragusin, and E. Neacsu, Radiological characterization plan for decommissioning IFIN-HH's Cyclotron, Progress in Nuclear Energy 168, (2024).

[38] S. Vichi, A. Infantino, F. Zagni, G. Cicoria, S. Braccini, D. Mostacci, and M. Marengo, Activation studies for the decommissioning of PET cyclotron bunkers by means of Monte Carlo simulations, Radiation Physics and Chemistry 174, (2020).

[39] H. S. Song and J. H. Cheong, Impact of Steel Equipment on Cyclotron Activation and Its Implications for Radioactive Waste Management, Nucl Technol (2025).

[40] H. Lee, S. Lee, D. Choi, G. Jeong, and H. Seo, Activation analysis of RFT-30 cyclotron target assembly, Radiation Physics and Chemistry 224, (2024).

[41] International Atomic Energy Agency, *Directory of Cyclotrons Used for Radionuclide Production in Member States, Update* (2006).

[42] IAEA, *IAEA Accelerator Knowledge Portal - Cyclotron Master List*, https://nucleus.iaea.org/sites/accelerators/Lists/Cyclotron Master List/cyclotrons_view_2020.aspx.

[43] A. Bosko, D. Zhilchenkov, and W. D. Reece, *GE PETtrace Cyclotron as a Neutron Source for Boron Neutron Capture Therapy*, in *Applied Radiation and Isotopes*, Vol. 61 (2004), pp. 1057–1062.

[44] M. A. S. Lacerda, D. A. M. Campolina, A. M. Guimarães, J. A. Benavente, and T. A. da Silva, Use of the MCNPX to calculate the neutron spectra around the GE-PETtrace 8 cyclotron of the CDTN/CNEN, Brazil, Applied Radiation and Isotopes 83, 235 (2014).

[45] J. A. Benavente-Castillo, M. A. S. Lacerda, A. V. Ferreira, H. M. Dalle, and T. A. Da Silva, Assessment of the neutron radiation field with activation foils and intermittent irradiations around a PETtrace biomedical cyclotron, Applied Radiation and Isotopes 153, 108823 (2019).

[46] M. Košťál et al., The methodology of characterization of neutron leakage field from PET production cyclotron for experimental purposes, Nucl Instrum Methods Phys Res A 942, 162374 (2019).

[47] IAEA, Cyclotron produced radionuclides Radionuclides: Guidelines for Setting Up a Facility, IAEA Technical Report 153 (2009).

[48] L. Hamidatou et al., Experimental determination and simulation of neutron and gamma flux parameters in horizontal channel for Prompt Gamma Neutron activation analysis implementation at Es-Salam research reactor, Applied Radiation and Isotopes 174, 109759 (2021).

[49] B. G. Park, B. J. Jun, G. D. Kang, M. S. Kim, H. J. Yoo, B. Y. Chung, and B. Lee, Measurement of the neutron flux distribution in a research reactor by neutron activation analysis, J Radioanal Nucl Chem 330, 501 (2021).

[50] C. A. Meert, A. P. Panter, A. J. Jinia, A. T. MacDonald, S. D. Clarke, B. D. Pierson, and S. A. Pozzi, High-fidelity photoneutron detection via neutron activation analysis, Nucl Instrum Methods Phys Res A 1040, 167116 (2022).

[51] S. H. Giegel, C. L. Pope, and A. E. Craft, Determination of the neutron energy spectrum of a radial neutron beam at a TRIGA reactor, Nucl Instrum Methods Phys Res B 454, 28 (2019).

[52] D. Lee, B. Bucher, K. Krebs, and E. Seabury, Determination of the Generator Neutron Flux Using Multi-Foil Neutron Activation Analysis Method, 2018.

[53] IAEA, Handbook on Nuclear Activation Cross-Sections, 1974.

[54] M. G. B. Mustafa Karadag, Haluk Yu¨cel, Measurement of thermal neutron cross section and resonance integral for (n , c) reaction in 152 Sm, Ann Nucl Energy 34, 188 (2007).

[55] S. Jan et al., GATE: A simulation toolkit for PET and SPECT, Phys Med Biol 49, 4543 (2004).

[56] K. Aoki, T. Kin, and N. Otuka, Nuclear data uncertainty in iterative neutron spectrum unfolding, J Nucl Sci Technol 59, 907 (2022).

[57] F. A. Abolaban et al., Estimation of Thermal & Epithermal Neutron Flux and Gamma Dose Distribution in a Medical Cyclotron Facility for Radiation Protection Purposes Using Gold Foils and Gate 9, Radiat Prot Dosimetry 193, 176 (2021).

[58] G. Healthcare, PETtrace 800 Series Site Planning Guide, (2013).

[59] M. A. Alawi, Y. Z. Hazzaa, R. B. Fawrah, F. M. Alhusini, A. M. Alhawsawi, and E. M. Banoqitah, *Characterization of the Direct and Scattered Neutron Flux Around Cyclotron Target*, in *Lecture Notes in Mechanical Engineering* (Springer Science and Business Media Deutschland GmbH, 2024), pp. 174–183.